Circular dichroism in photoelectron images from aligned nitric oxide molecules

Ananya Sen, S. T. Pratt, and K. L. Reid

Circular dichroism in photoelectron images from aligned nitric oxide molecules

Ananya Sen,[1] S. T. Pratt,[1] and K. L. Reid[2]
[1]*Argonne National Laboratory, Argonne, Illinois 60439, USA*
[2]*School of Chemistry, University of Nottingham, Nottingham NG7 2RD, United Kingdom*

We have used velocity map photoelectron imaging to study circular dichroism of the photoelectron angular distributions (PADs) of nitric oxide following two-color resonance-enhanced two-photon ionization via selected rotational levels of the A $^2\Sigma^+$, $v' = 0$ state. By using a circularly polarized pump beam and a counter-propagating, circularly polarized probe beam, cylindrical symmetry is preserved in the ionization process, and the images can be reconstructed using standard algorithms. The velocity map imaging set up enables individual ion rotational states to be resolved with excellent collection efficiency, rendering the measurements considerably simpler to perform than previous measurements conducted with a conventional photoelectron spectrometer. The results demonstrate that circular dichroism is observed even when cylindrical symmetry is maintained, and serve as a reminder that dichroism is a general feature of the multiphoton ionization of atoms and molecules. The observed PADs are in good agreement with calculations based on parameters extracted from previous experimental results obtained by using a time-of-flight electron spectrometer. *Published by AIP Publishing.* [http://dx.doi.org/10.1063/1.4982218]

I. INTRODUCTION

Photoelectron circular dichroism (PECD) is a measure of the difference between the photoelectron angular distributions (PADs) following photoionization by left circularly polarized (LCP) and right circularly polarized (RCP) light.[1–3] In the literature, this effect has been taken to refer to a forward-backward asymmetry in photoelectron intensity which reverses on changing the helicity of the light. In the electric dipole approximation, such an asymmetry can only be observed for molecules that are oriented in space[4,5] or that are chiral.[6–8] For chiral molecules, PECD effects of 10% or larger are common, and PECD is becoming a popular tool for the study of chiral systems. Both single-photon and multiphoton ionization have been used to generate PECD signals, and the technique has been demonstrated with continuous (cw) sources (such as synchrotron radiation) and with pulsed laser sources, using pulses as short as a few fs.[1–3] The development of efficient, high-speed imaging detectors has been particularly beneficial to the development of PECD techniques.

For a randomly oriented sample of nonchiral molecules (or for a racemic mixture), the PECD signal will be zero. However, if the sample molecules (or even atoms) are aligned or oriented, a dichroic effect in the PADs can be observed.[9] Because this effect does not result in a forward-backward asymmetry it is termed as "CDAD" (circular dichroism in photoelectron angular distributions)[9] in order to distinguish it from PECD. About 30 years ago, Dubs *et al.* developed a theoretical framework to describe CDAD in situations in which a sample of aligned molecules was probed by ionization with LCP and RCP light.[9] Their formalism enabled the alignment of the sample to be extracted from the CDAD signal. Experimental

demonstrations of this approach were reported by Appling *et al.*[10,11] soon thereafter. In their experiments, a linearly polarized pump laser was used to populate and align the A $^2\Sigma^+$ state of NO via a one- or two-photon transition. The alignment created by the pump transition was then characterized by ionizing the A $^2\Sigma^+$ state with LCP and RCP light. In these experiments, the photoelectron spectra were vibrationally, but not rotationally, resolved and the circular dichroism effect in the photoelectron angular distributions reached 15%-20% in some cases.[10,11]

In the early 1990s, Zare and co-workers published a series of papers[5,12–16] on rotationally resolved photoelectron angular distributions following resonant, two-photon ionization via selected rotational levels of the A $^2\Sigma^+$ state of NO. Rather than using CDAD to characterize the alignment of the A $^2\Sigma^+$ state, they showed that the CDAD signal corresponding to rotationally resolved levels of the ion could be used to extract not only the transition moments and phase shifts between photoelectron partial waves but also the signs of these phase shifts. This advance made this photoionization measurement "complete."[13,16]

While the development of imaging techniques has led to a tremendous growth in PECD studies,[1–3] the use of CDAD to extract photoionization parameters from photoelectron angular distributions has remained relatively under-developed. One reason for this situation is that in the CDAD geometries used in previous works,[5,10–16] the cylindrical symmetry of the system is broken, and thus reconstruction methods that rely on this symmetry can no longer be applied. In the present study, we investigate the possibility of using photoelectron angular distributions generated by counter-propagating circularly polarized pump and probe beams to access information about the photoionization dynamics. This approach preserves

the cylindrical symmetry of the system, allowing standard reconstruction methods, and is considerably simpler than the previous approach. The experimental geometry is the same as that used in PECD experiments on chiral molecules and thus the CDAD we observe will also contribute to PADs measured in those experiments. We demonstrate the method by application to the A $^2\Sigma^+$ state of NO, by measuring photoelectron images which have structure corresponding to resolved ion rotational states. This enables the comparison of the results with those from the earlier measurements.[12,16]

II. EXPERIMENT

We will briefly summarize the experimental setup, which has been described in more detail previously.[17–19] The imaging apparatus consists of a source chamber and a detection chamber separated by a 2 mm skimmer. A mixture of 5% NO in He with a backing pressure of ~2 atm is introduced into the chamber via a pulsed valve to produce a molecular beam. The axis of the molecular beam is colinear with the time-of-flight axis of the imaging spectrometer. The timing of the molecular beam pulse was synchronized with the laser pulses and the detection electronics by using a series of digital delay generators. The timing was adjusted to sample the beginning of the gas pulse to minimize cluster formation and to provide a relatively warm sample. This approach allowed us to access higher rotational states of NO in the pump transition, which reduces the difficulty of recording rotationally resolved photoelectron images.

The two laser pulses were produced by using two independent Nd:YAG-pumped dye lasers. The pump beam was generated by frequency doubling the 452 nm output of the first dye laser to produce linearly polarized light at ~226 nm to excite individual rotational lines of the one-photon A $^2\Sigma^+$, v' = 0 ← X $^2\Pi$, v'' = 0, transition in NO.[20–22] The probe beam was produced by frequency doubling the 624–653 nm output of the second laser to produce linearly polarized light between ~312 and 330 nm. For the images reported here, the probe laser was fixed at 326 nm. The wavelengths of both the pump and probe were calibrated using a commercial wavemeter, and the wavemeter was also checked by comparing readings for the pump laser with the known transition energies for the A $^2\Sigma^+$, v' = 0 ← X $^2\Pi$, v'' = 0 band.[20–22] The pump and probe beams entered the interaction region from opposite sides of the chamber, i.e., in a counter-propagating colinear geometry. Typically, the pulse energy of the pump beam was a few μJ, while that of the probe was 10-100 μJ. The pulses from the pump and probe lasers had widths of ~8 ns, and the timing was adjusted so that the probe pulse arrived in the interaction region ~0–4 ns after the pump pulse. In principle, hyperfine depolarization could influence the observed circular dichroism signal; however, as discussed by Appling *et al.*,[10,11] such hyperfine effects are expected to be negligible for the high-*J* levels accessed in the present work. Both the pump and probe beams were loosely focused into the interaction region.

The linear polarization of the pump beam was purified by using an air-spaced Rochon polarizer. Circularly polarized light was then produced by using a zero-order quarter-wave plate. Similarly, the linearly polarized light of the probe laser beam was converted to circularly polarized light by using a second zero-order quarter-wave plate. The circular polarization of each beam was checked by passing it through a linear polarizer and the quarter-wave plate, and then back-reflecting the resulting beam through the quarter-wave plate and polarizer. The circular polarization produced by the first pass through quarter-wave plate is reversed on back reflection, with the result that after passing back through the quarter-wave plate, the polarization is linear and rotated by 90° with respect to the input linear polarized light. Thus, if the quarter-wave plate is generating circularly polarized light, the back-reflected beam is rejected by the polarizer.

To a molecule in the molecular beam, the polarization of a LCP laser beam propagating from left to right looks the same as the polarization of a RCP beam propagating from right to left. Thus, there is potential for confusion in labeling the polarizations with counter-propagating pump and probe beams. To avoid any potential confusion, in what follows, the polarizations of both the pump and probe beams are always specified as if they are propagating colinearly in the direction of the pump beam.

The pump and probe laser beams intersected the molecular beam just downstream of the skimmer, between the repeller and extractor plates of a conventional, magnetically shielded velocity-map imaging (VMI) spectrometer.[17,19–23] The photoelectrons created in the interaction region are imaged onto a microchannel plate connected to a phosphor screen. A video camera is synchronized to the laser timing and interfaced to a computer, which captures the resulting photoelectron images. Selective gating of voltages on detectors minimizes background electrons in the image. Each image is signal averaged for 20 000 laser pulses. The photoelectron images, shown later in this paper, are a sum of four such signal-averaged images. The images were reconstructed by using the pBASEX program.[24] With circularly polarized pump and probe beams, cylindrical symmetry is preserved around the propagation axis of the laser beams, so that the pBASEX routine is still appropriate.

The tuning of repeller and extractor voltages is important to achieve the best performance of the imaging spectrometer. The ratio between these two voltages defines the field in the interaction region. The electric field in the interaction region was inhomogeneous and was maintained roughly between 20 and 30 V/cm. Minimizing the signal from electrons generated by scattered light from the pump and particularly the probe beams was also important for recording the best images. We found that tuning the spectrometer to achieve spatial focusing of the electrons (i.e., with only a small difference in the repeller and extractor voltages) was very helpful in this task, as it allowed the determination of where the scattered light was generating electrons. The alignment of the pump and probe beams could then be adjusted accordingly to minimize the scattered signal while preserving the signal of interest. While background images were recorded and subtracted from the full images in some of the experiments, this did not significantly affect the quality of the resulting images,

and no background images were subtracted for most of the data.

In the present experiment, we investigate two-color, two-photon ionization of NO via the A $^2\Sigma^+$, v′ = 0 state, which has been characterized previously in considerable detail. Here, the pump laser excited individual rotational levels, A $^2\Sigma^+$, v′ = 0, N′ of the intermediate state.[20–22] The spin-orbit splitting of the X $^2\Pi$ state is ~120 cm^{-1},[21] and we focus on transitions from the lower (F$_1$) $^2\Pi_{1/2}$, v″ = 0, J″ = N″ + 1/2 component. Note that each rotational level of the $^2\Pi_{1/2}$ state is split into ± parity levels as a result of Λ doubling. As is characteristic of Hund's case (b), each of the A $^2\Sigma^+$, v′ = 0, N′ levels is split into F$_1$ and F$_2$ components with J′ = N′ + 1/2 and N′ − 1/2, respectively, with both having the same ± parity. This spin splitting in the A $^2\Sigma_u^+$ state depends on N′, but is less than 0.1 cm^{-1} for the rotational levels of interest,[22] and is not resolved in the present experiments. In what follows, pump transitions are labeled as $\Delta J_{F'F''}(J'')$. As a result of the small spin splitting in the A $^2\Sigma^+$ state, there is some overlap in the pump transitions used in the present study. In particular, the R$_{11}(J'')$ and Q$_{21}(J'')$ transitions are blended, as are the Q$_{11}(J'')$ and P$_{21}(J'')$ transitions.

Previous studies have shown that the A $^2\Sigma^+$ state of NO is nearly a pure gerade state.[25] Indeed, a single-center expansion of the 3sσ orbital around the center of mass yields approximately 94% s character, 0.3% p character, and 5% d character.[25] In spherical symmetry, the photoionizing transition will have l − l′ = Δl = ±1, where l and l′ are the orbital angular momenta of the Rydberg orbital and ejected photoelectron, respectively. Furthermore, for ionization from a $^2\Sigma^+$ intermediate state into the continuum of a $^1\Sigma^+$ ion state, transitions with N$^+$ − N′ = ΔN = even must be associated with odd-l photoelectrons, and transitions with ΔN = odd must be associated with even-l photoelectrons.[26] Thus, based on the character of the intermediate state, the dominance of photoelectrons with odd l and photoionizing transitions with ΔN = even is expected. This expectation is consistent with previous rotationally resolved photoelectron spectra for the direct photoionization of the A $^2\Sigma^+$ state, in which the ΔN = 0 transition is most intense, followed by much weaker ΔN = ±2 transitions and even weaker ΔN = ±1 transitions. In principle, larger values of ΔN are possible with the ejection of l ≥ 2 photoelectrons, but such features are generally too weak to be observed.

III. THEORETICAL BACKGROUND

We use the theoretical framework for describing rotationally resolved photoelectron angular distributions for direct two-color, resonance-enhanced two-photon ionization of NO via the A $^2\Sigma^+$ state that was developed by McKoy and co-workers[27] and extended by Zare and co-workers.[13,16] The relevant parts of this framework are described only briefly in what follows. For the case of two-photon ionization with two co-(or counter-)propagating circularly polarized laser beams, cylindrical symmetry is maintained and the angle-resolved photoelectron intensity can be expressed as[28]

$$I(\theta, \phi) = B_{00}Y_{00}(\theta, \phi) + B_{20}Y_{20}(\theta, \phi) + B_{40}Y_{40}(\theta, \phi)$$
$$= \beta_{00}\{1 + \beta_{20}Y_{20}(\theta, \phi) + \beta_{40}Y_{40}(\theta, \phi)\}. \quad (1)$$

In Eq. (1) $Y_{LM}(\theta, \phi)$ are spherical harmonics, β_{00} is proportional to the angle-integrated photoelectron intensity, and β_{20} and β_{40} are normalized anisotropy parameters. Following the formalism given in Ref. 15, the B_{L0} parameters can be expressed as

$$B_{L0} = \frac{1}{\sqrt{4\pi}} \sum_{ll'} \sum_{\lambda\lambda'} \sum_m C(N^+, L, l, \lambda, l', \lambda', m) r_{l\lambda} r_{l'\lambda'}$$
$$\times \cos(\eta_{l\lambda} - \eta_{l'\lambda'}), \quad (2)$$

where N^+ is the rotational angular momentum quantum number of the ion state formed. According to Eq. (2), the B_{L0} (and hence β_{L0}) parameters depend on geometrical factors, $C(N^+, L, l, \lambda, l', \lambda', m)$, that depend on angular momentum coupling in the excitation and ionization steps, multiplied by a dynamical factor, $r_{l\lambda}r_{l'\lambda'}\cos(\eta_{l\lambda} - \eta_{l'\lambda'})$, that contains the radial dipole matrix elements, $r_{l\lambda}$, connecting the ionized state to each possible photoelectron (l, λ) partial wave, and the phase difference $\eta_{l\lambda} - \eta_{l'\lambda'}$, between pairs of partial waves.[15] Because cylindrical symmetry is maintained, the projection, m, of l onto the laboratory frame axis (the light propagation direction in this case) has to be the same for both l and l′. Expressions for the geometrical factors, which depend on the rotational level of the A $^2\Sigma^+$ state as well as that of the ion, can be found in Ref. 15; these can be readily calculated using available software routines for angular momentum coupling coefficients. Simulation of the photoelectron angular distributions therefore can be achieved with knowledge of the radial dipole matrix elements and phases contained in Eq. (2).

In the case of ionization of NO A $^2\Sigma^+$, it has been shown that it is possible to extract values for $r_{l\lambda}$ and $\eta_{l\lambda}$ directly from rotationally resolved experimental measurements of photoelectron angular distributions.[12,13,16] The rotational resolution serves to enhance the sensitivity to the dynamical parameters, which depend in general on the vibrational state ionized and on the photoelectron kinetic energy, although it is likely that this dependence is weak. For example, the dynamical parameters resulting from the ionization of the A $^2\Sigma^+$ (v′ = 1) state have been shown to be very similar to those resulting from the ionization of the A $^2\Sigma^+$ (v′ = 0) state.[13,16] In Ref. 16

TABLE I. Dynamical parameters (radial dipole matrix element and phases) used in the simulation of the photoelectron angular distributions.[a]

l	λ	Wave	$r_{l\lambda}$ (normalised)	$\eta_{l\lambda}$ (rad)
0	0	sσ	0.204	0
1	0	pσ	0.503	0
1	±1	pπ	0.471	0.216
2	0	dσ	0.166	−2.740
2	±1	dπ	0.073	−3.926
2	±2	dδ	0	0
3	0	fσ	0.321	−1.029
3	±1	fπ	0.244	−1.046
3	±2	fδ	0	0
3	±3	fφ	0	0

[a]All values were taken from Ref. 16.

an ionizing wavelength of 313.5 nm was used to ionize NO from its A $^2\Sigma^+$ (v' = 0, N = 22) state. The resulting photoelectrons had a kinetic energy of ~0.17 eV when the N^+ = 22 ion state was formed, i.e., following the $\Delta N = 0$ transition. By comparison, the equivalent photoelectrons in the present work were released with ~0.03 eV kinetic energy. In the absence of a near-threshold resonance it is unlikely that the radial dipole matrix elements and phases will vary significantly over this energy range and so the parameters from Ref. 16 were used in the simulations presented here. This set of parameters is listed in Table I. Finally, we note that the calculations were performed by assuming that the X $^2\Pi$ state corresponds to pure Hund's case (b), and they do not account for the two overlapping pump transitions. The potential implications of this approximation are discussed below.

IV. RESULTS AND DISCUSSION

A. Two-color photoelectron images

Figures 1 and 2 show raw and reconstructed photoelectron images obtained following one-photon excitation with LCP light of the NO A $^2\Sigma^+$, v' = 0, N' = 15 level via the overlapped $R_{11}(14.5)$ and $Q_{21}(14.5)$ transitions, followed by one-photon ionization at 326 nm into the NO$^+$ X $^1\Sigma^+$ continuum. At this probe wavelength, only a single vibrational level of the ion can be populated, and the observed rings correspond to the population of different rotational levels of the X $^1\Sigma^+$, v$^+$ = 0 ion. The probe beam was RCP for the images shown in Figure 1 and LCP for the images shown in Figure 2.

In both Figures 1 and 2, five rings are observable, corresponding, from small to large radius, to ionization processes with $\Delta N = 2, 1, 0, -1,$ and -2, respectively. The dominant ring in both figures corresponds to the $\Delta N = 0$ process. The raw and reconstructed images for the two polarization configurations show qualitative and quantitative differences in the relative intensities of different rings and in the angular distributions of these rings. For example, the intensity of the innermost ($\Delta N = 2$) ring in Figure 1 is peaked in the direction perpendicular to the laser propagation direction, while the intensity of the same ring in Figure 2 is more isotropic and is actually slightly more intense along the propagation axis. Such differences are a clear signal of circular dichroism and will be discussed in more detail in Sections IV B and IV C.

Figure 3 shows the raw and reconstructed images obtained for the same pump and probe wavelengths used in Figures 1 and 2, but with both beams linearly polarized. For Figure 3, the pump and probe share the same linear polarization axis, which is aligned perpendicular to the plane of the detector. This configuration allows the use of standard reconstruction methods. Figure 3 shows the same five rings as Figures 1 and 2, but there is little variation of the angular distributions with ΔN. Photoelectron images were also recorded for all three polarization configurations following excitation via the overlapped $Q_{11}(16.5)$ + $P_{21}(16.5)$ transitions. The raw and reconstructed images are shown in Figures S1–S3 of the supplementary material, and the corresponding rotational branching ratios

and photoelectron angular distributions are also discussed in Sections IV B and IV C.

B. Photoelectron spectra

The velocity map imaging spectrometer has essentially 4π collection efficiency, and the integration of the reconstructed images of Figures 1–3 with respect to θ results in photoelectron spectra in which the peak intensities reflect the relative branching fractions for the different rotational final states. Figure 4 shows the photoelectron spectra for the $R_{11}(14.5)$ + $Q_{21}(14.5)$ pump transition recorded with three different polarization combinations of the pump and probe beams. The corresponding photoelectron spectra recorded for the $Q_{11}(16.5)$ + $P_{21}(16.5)$ pump transition are shown in Figure S4 of the supplementary material. For both pump transitions, the $\Delta N = 0$ feature is by far the most intense
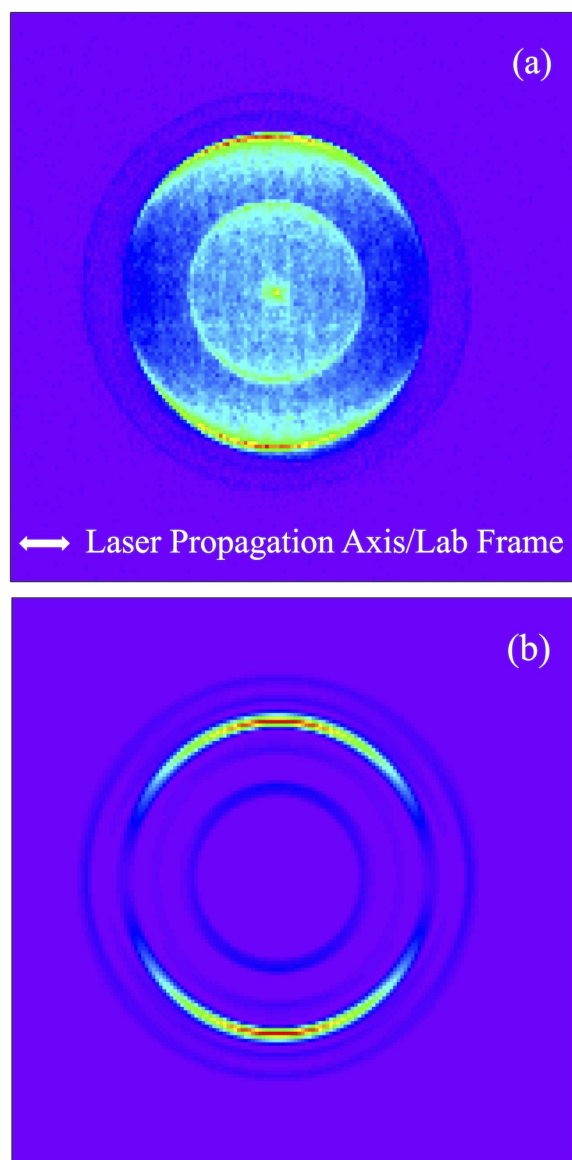

FIG. 1. (a) The raw photoelectron image recorded following excitation via the A $^2\Sigma^+$, v' = 0 ← X $^2\Pi$, v'' = 0, $R_{11}(14.5)$ + $Q_{21}(14.5)$ transition and ionization at 326 nm. Here the pump laser is LCP and probe laser is *RCP*. (b) The reconstructed image from (a).

FIG. 2. (a) The raw photoelectron image recorded following excitation via the A $^2\Sigma^+$, v' = 0 ← X $^2\Pi$, v'' = 0, $R_{11}(14.5)$ + $Q_{21}(14.5)$ transition and ionization at 326 nm. Here the pump laser is LCP and probe laser is *LCP*. (b) The reconstructed image from (a).
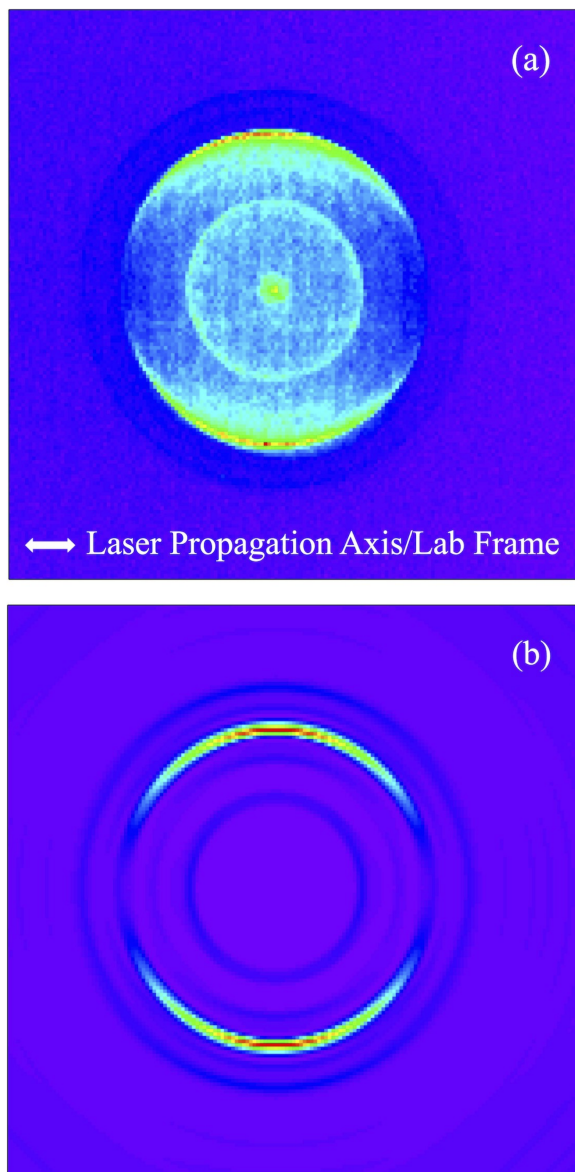

FIG. 3. (a) The raw photoelectron image recorded following excitation via the A $^2\Sigma^+$, v' = 0 ← X $^2\Pi$, v'' = 0, $R_{11}(14.5)$ + $Q_{21}(14.5)$ transition and ionization at 326 nm. Here the polarizations of the pump and probe lasers are *linear and parallel to each other*. (b) This is a reconstructed photoelectron image from (a).

in each photoelectron spectrum, while the $\Delta N = \pm 1$ features are the weakest. This behavior is independent of the polarizations of the pump and probe beams and is consistent with the 3s character of the intermediate state and the discussion presented in Section II. In particular, the expected dominance of l = odd photoelectrons results in a corresponding dominance of ΔN = even peaks in the photoelectron spectra.

Branching ratios to each of the rotationally resolved ion states were determined for each of the spectra shown in Figure 4 by integrating the intensity over each photoelectron peak and normalizing the intensity to that of the $\Delta N = 0$ peak. These branching ratios are given in Table II. Table III shows the corresponding branching ratios for spectra recorded by using the $Q_{11}(16.5)$ + $P_{21}(16.5)$ pump transition. The error bars were determined by comparing the branching fractions
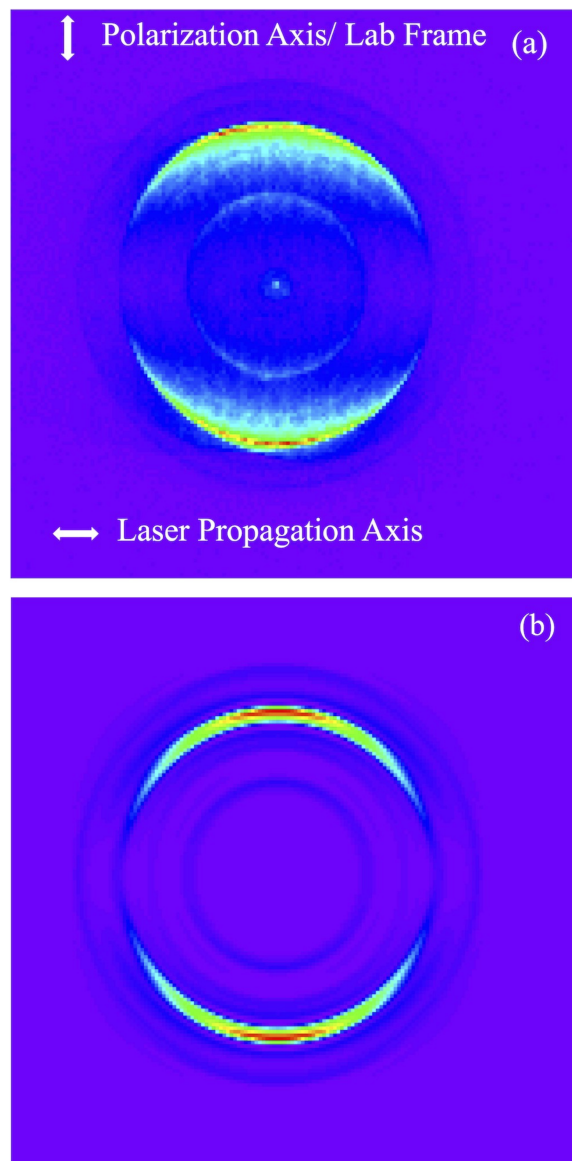
of the summed image with the branching fractions determined from the corresponding set of individual images. Also shown in Tables II and III are the predicted branching ratios based on the complete set of parameters determined by Leahy *et al.*[16] and provided in Table I. Overall, the qualitative agreement between the experimental and theoretical branching ratios is good, although there are some larger discrepancies for the weakest peaks corresponding to the $\Delta N = \pm 1$ processes.

The experimental rotationally resolved branching ratios for the $R_{11}(14.5)$ + $Q_{21}(14.5)$ pump transition show a distinct circular dichroism. In particular, for the RCP probe spectrum, the intensity of the $\Delta N = +2$ peak is approximately twice that of the $\Delta N = -2$ peak, while for the LCP probe spectrum, the intensity of the $\Delta N = +2$ peak is approximately 0.7 times that of the $\Delta N = -2$ peak. These observations are qualitatively
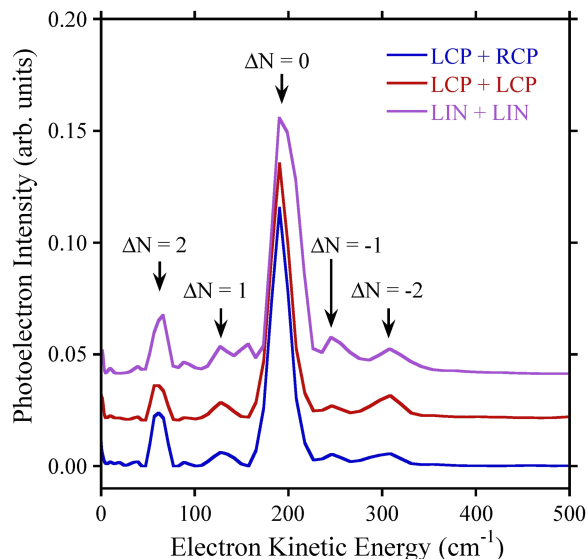
FIG. 4. The photoelectron spectra resulting from the reconstructed image recorded following excitation via the A $^2\Sigma^+$, v' = 0 ← X $^2\Pi$, v'' = 0, $R_{11}(14.5) + Q_{21}(14.5)$ transition and ionization at 326 nm. Spectra are shown for three polarization combinations: LCP pump + RCP probe, LCP pump + LCP probe, and LIN pump + LIN probe. The polarizations of the LIN pump and probe are parallel to each other.

consistent with the predictions based on the parameters given in Table I which give a $\Delta N = +2$ to $\Delta N = -2$ ratio of 3.1 for the RCP probe and 0.4 for the LCP probe. The theory also predicts a significant dichroism with respect to the $\Delta N = \pm 1$ peaks. In particular, the predicted ratio of the $\Delta N = +1$ to -1 intensities shifts from 0.5 with a RCP probe to 2.1 with a LCP probe. This effect is not observed in the experimental $\Delta N = \pm 1$ peaks, which may simply be due to uncertainties resulting from their small intensities.

The observed dichroism in the rotational branching ratios is consistent with the observations of Leahy et al.,[5] who saw changes in the rotational branching ratios when using linearly polarized light and switching from a parallel to perpendicular geometry. In that case, however, the dichroism was most pronounced for the $\Delta N = 0$ transition. Interestingly, very little dichroism in the rotationally resolved branching ratios is predicted for spectra recorded by using the $Q_{11}(16.5) + P_{21}(16.5)$

TABLE II. Rotational branching ratios obtained following excitation via the A $^2\Sigma^+$, v' = 0 ← X $^2\Pi$, v'' = 0, $R_{11}(14.5) + Q_{21}(14.5)$ transition and ionization at 326 nm. The intensity of each ΔN photoelectron peak was determined by integrating the area of the respective PES peak. Theoretical values were determined by using the parameters described in Section III. The error bars were determined by comparing the branching fractions of the summed image with the branching fractions determined from the corresponding set of individual images.

	$R_{11}(14.5) + Q_{21}(14.5)$					
ΔN	LCP-RCP expt.	LCP-RCP theory	LCP-LCP expt.	LCP-LCP theory	LIN-LIN expt.	LIN-LIN theory
−2	0.08(1)	0.06	0.14(1)	0.16	0.15(1)	0.12
−1	0.05(1)	0.06	0.07(1)	0.03	0.14(1)	0.05
0	1	1	1	1	1	1
1	0.06(1)	0.03	0.07(1)	0.07	0.09(1)	0.06
2	0.16(1)	0.18	0.10(1)	0.07	0.13(1)	0.13

TABLE III. Rotational branching ratios obtained following excitation via the A $^2\Sigma^+$, v' = 0 ← X $^2\Pi$, v'' = 0, $Q_{11}(16.5) + P_{21}(16.5)$ transition and ionization at 326 nm. The intensity of each ΔN photoelectron peak was determined by integrating the area of the respective PES peak. Theoretical values were determined by using the parameters described in Section III.

	$Q_{11}(16.5) + P_{21}(16.5)$					
ΔN	LCP-RCP expt.	LCP-RCP theory	LCP-LCP expt.	LCP-LCP theory	LIN-LIN expt.	LIN-LIN theory
−2	0.13(1)	0.10	0.13(1)	0.11	0.15(1)	0.09
−1	0.08(1)	0.04	0.07(1)	0.04	0.13(1)	0.03
0	1	1	1	1	1	1
1	0.09(1)	0.04	0.08(1)	0.05	0.08(1)	0.03
2	0.11(1)	0.12	0.12(1)	0.12	0.12(1)	0.11

pump transition. The experimental data in Table III support this prediction.

C. Photoelectron angular distributions

The reconstruction of a photoelectron image by using the pBASEX program[24] yields three b_L parameters: b_0, b_2, and b_4, which are coefficients of the Legendre polynomials $P_L(\cos\theta)$, where $L = 0$, 2, and 4. These b_L values are then weighted by the photoelectron intensity and integrated over the separate ranges of radius in the images corresponding to the observed ΔN rings. The resulting b_L values are converted to the B_{00}, B_{20}, and B_{40} coefficients in Equation (1) by dividing by $\sqrt{2L + 1}$. B_{20} and B_{40} are then converted to the normalized β_{20} and β_{40} values of Equation (1) by dividing by β_{00}. The experimental β_{LM} values derived from ionization via the $R_{11}(14.5) + Q_{21}(14.5)$ transition and $Q_{11}(16.5) + P_{21}(16.5)$ transition are given in Tables IV and V for the three combinations of pump and probe polarization (LCP pump/RCP probe, LCP pump/LCP probe, and linear pump/linear probe). The error bars listed are those output by the pBASEX image inversion program.[24] These error bars depend on both the intensity of the feature and on how well the angle-resolved photoelectron intensity is fitted by Eq. (1) but nonetheless generally appear to underestimate the likely error bars which are not easily determined by any other method. Also shown in Tables IV and V are the theoretical β_{LM} values obtained by using the complete set of parameters extracted previously from experiments by Leahy et al.[16] and listed in Table I. As mentioned above, the theoretical values were calculated assuming that the X $^2\Pi$ state corresponds to pure Hund's case (b) and does not account for the two overlapping pump transitions. As a result, the alignment created in the experiment by the blended pump transition will be somewhat reduced from the alignment used in the calculations, and consequently the corresponding PAD anisotropy will be lower. As we will see below, the good agreement between the experimental and calculated PADs indicates that this reduction is small.

While the comparison of the experimental and predicted rotational branching ratios is relatively straightforward, it is somewhat harder to visualize the differences between the experimental and predicted angular distributions based on a table of the β_{LM} values. However, the normalized photoelectron angular distributions can be visualized as polar plots of

TABLE IV. The angular distribution parameters, β_{LM} [Eq. (1)], obtained following excitation via the A $^2\Sigma^+$, $v' = 0 \leftarrow$ X $^2\Pi$, $v'' = 0$, $R_{11}(14.5) + Q_{21}(14.5)$ transition and ionization at 326 nm. The terms LCP, RCP, and LIN correspond to left circular, right circular, and linear polarization. The notation of the polarization corresponds to pump polarization-probe polarization. The error bars on β_{20} and β_{40} are those generated by the pBASEX reconstruction algorithm.[24]

| | | $R_{11}(14.5) + Q_{21}(14.5)$ | | | | | |
| | | LCP-RCP expt. | LCP-RCP theory | LCP-LCP expt. | LCP-LCP theory | LIN-LIN expt. | LIN-LIN theory |
	Parameters						
$\Delta N = -2$	β_{00}	7.8	5.8	14.2	16.2	15.2	11.6
	β_{20}	0.059(20)	0.557	−0.200(10)	−0.369	0.182(10)	0.129
	β_{40}	0.002(20)	0.045	0.026(10)	0.016	−0.085(10)	0.090
$\Delta N = -1$	β_{00}	5.2	6.5	6.9	3.1	13.7	5.4
	β_{20}	−0.325(20)	−0.360	−0.218(10)	−0.419	0.462(10)	0.781
	β_{40}	−0.008(20)	0.008	−0.013(10)	0.016	−0.371(10)	0.036
$\Delta N = 0$	β_{00}	100	100	100	100	100	100
	β_{20}	−0.507(1)	−0.396	−0.427(1)	−0.399	0.871(2)	0.792
	β_{40}	0.066(1)	−0.013	0.018(1)	−0.013	0.085(1)	−0.050
$\Delta N = 1$	β_{00}	5.6	3.5	6.6	6.7	8.6	5.6
	β_{20}	−0.282(20)	−0.410	−0.263(10)	−0.360	0.376(10)	0.781
	β_{40}	0.036(10)	0.013	0.033(10)	0.007	−0.041(10)	0.031
$\Delta N = 2$	β_{00}	16	18.2	9.9	6.9	12.9	13.1
	β_{20}	−0.189(3)	−0.350	0.147(10)	0.507	0.169(4)	0.127
	β_{40}	−0.008(3)	0.0136	−0.006(10)	0.036	−0.005(3)	0.075

photoelectron intensity in which the angle, θ, is the angle between the propagation (circularly polarized light) or polarization (linearly polarized light) axis of the light and the detection direction of the photoelectron, and the radius, R,

is proportional to the photoelectron band intensity at that angle. Figure 5 shows the rotationally resolved photoelectron angular distributions for photoionization via the $R_{11}(14.5)$ + $Q_{21}(14.5)$ transition with a LCP pump beam and RCP

TABLE V. The angular distribution parameters obtained following excitation via the A $^2\Sigma^+$, $v' = 0 \leftarrow$ X $^2\Pi$, $v'' = 0$, $Q_{11}(16.5) + P_{21}(16.5)$ transition and ionization at 326 nm. The terms LCP, RCP, and LIN correspond to left circular, right circular, and linear polarization. The notation of the polarization corresponds to pump polarization-probe polarization. The error bars on β_{20} and β_{40} are those generated by the pBASEX reconstruction.

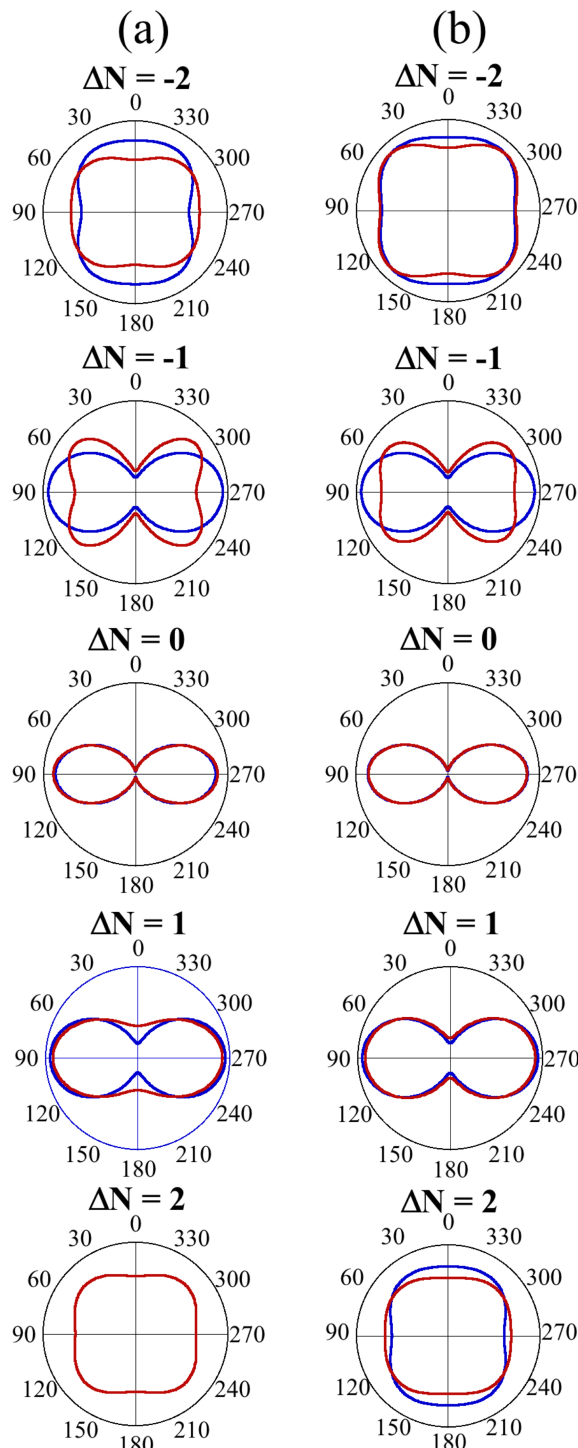| | | $Q_{11}(16.5) + P_{21}(16.5)$ | | | | | |
| | | LCP-RCP expt. | LCP-RCP theory | LCP-LCP expt. | LCP-LCP theory | LIN-LIN expt. | LIN-LIN theory |
	Parameters						
$\Delta N = -2$	β_{00}	13.4	10.1	12.5	10.8	14.7	9.3
	β_{20}	−0.027(20)	0.111	0.017(20)	0.055	0.131(10)	0.063
	β_{40}	−0.043(20)	−0.047	−0.063(10)	−0.044	−0.170(10)	−0.207
$\Delta N = -1$	β_{00}	7.9	4.3	7.4	4.1	13.2	3.1
	β_{20}	−0.091(10)	−0.318	−0.141(10)	−0.318	0.396(10)	0.517
	β_{40}	−0.155(10)	−0.021	−0.124(10)	−0.022	−0.404(10)	−0.117
$\Delta N = 0$	β_{00}	100	100	100	100	100	100
	β_{20}	−0.469(2)	−0.452	−0.442(2)	−0.452	0.841(2)	0.910
	β_{40}	0.039(1)	0.023	0.022(1)	0.023	0.057(1)	0.092
$\Delta N = 1$	β_{00}	8.9	4.5	8.2	4.6	7.6	3.5
	β_{20}	−0.249(20)	−0.323	−0.286(10)	−0.323	0.310(10)	0.532
	β_{40}	0.017(20)	−0.018	−0.018(10)	−0.017	−0.053(10)	−0.092
$\Delta N = 2$	β_{00}	11	12.2	12	11.5	11.6	10.7
	β_{20}	0.020(10)	0.033	−0.005(10)	0.085	0.144(5)	0.070
	β_{40}	−0.051(10)	−0.037	−0.033(10)	−0.039	−0.069(4)	−0.169
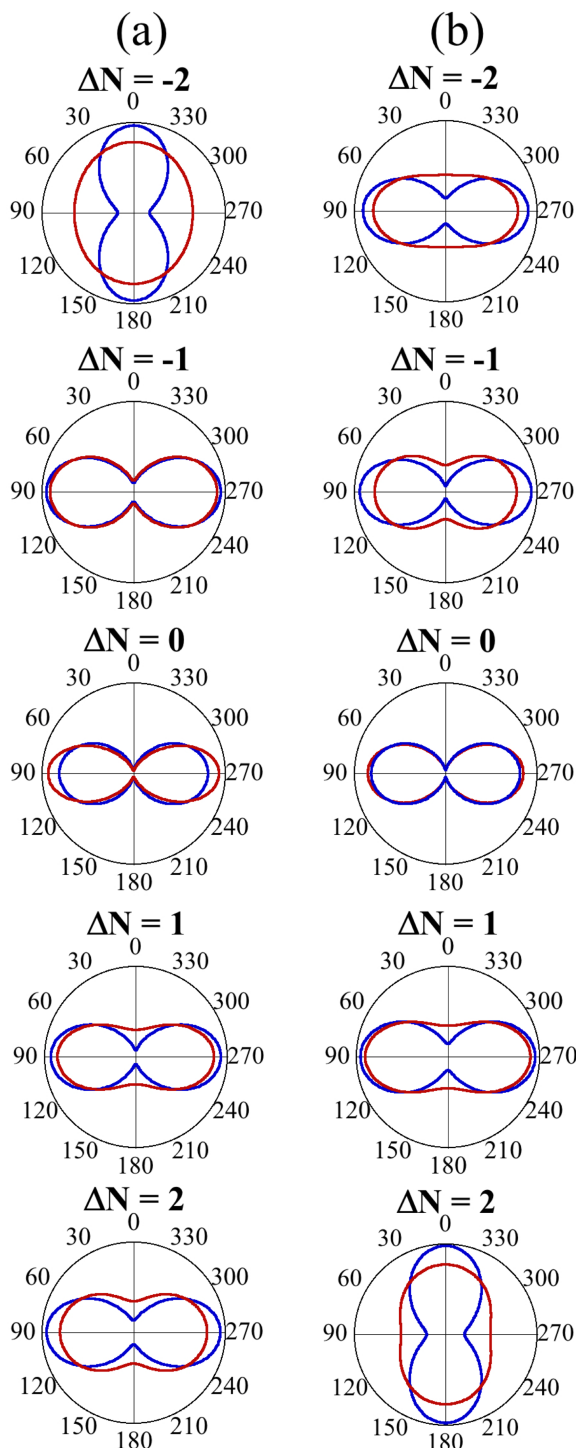
FIG. 5. (a) The PADS following excitation via the A $^2\Sigma^+$, v' = 0 ← X $^2\Pi$, v'' = 0, $R_{11}(14.5) + Q_{21}(14.5)$ transition and ionization at 326 nm with the LCP pump beam and RCP probe beam. The experimental distributions are shown in red and the theoretical distributions are shown in blue. (b) PADS following the same excitation process but with a LCP probe beam.

FIG. 6. (a) The PADS following excitation via the A $^2\Sigma^+$, v' = 0 ← X $^2\Pi$, v'' = 0, $Q_{11}(16.5) + P_{21}(16.5)$ transition and ionization at 326 nm with the LCP pump beam and RCP probe beam. The experimental distributions are shown in red and the theoretical distributions are shown in blue. In some cases, the experimental distribution is so similar to the theoretical distribution that the latter disappears from view. (b) PADS following the same excitation process but with a left circularly polarized probe beam.

and LCP probe beams. Figure 6 shows the corresponding angular distributions for the $Q_{11}(16.5) + P_{21}(16.5)$ transition. In these figures, the experimental angular distributions are shown in red, and the theoretical angular distributions are shown in blue.

In Figure 5, the PADs for the $R_{11}(14.5) + Q_{21}(14.5)$ pump transition display a number of interesting features. Overall,

there is excellent agreement between the experimental and theoretical rotationally resolved photoelectron angular distributions. Neither the $\Delta N = 0$ nor ±1 PADs in Figure 5 show significant dichroism in either the experiment or the theoretical angular distributions. These distributions, particularly the theoretical ones, have strong "p-like" character and are

peaked perpendicular to the propagation direction of the laser beams. In contrast, the $\Delta N = \pm 2$ PADs show a strong polarization dependence, with the LCP/LCP distribution for $\Delta N = +2$ looking like the LCP/RCP distribution for $\Delta N = -2$, and vice versa. Specifically, for the RCP probe, the distribution is peaked perpendicular to the propagation direction for $\Delta N = +2$ and parallel to it for $\Delta N = -2$; in contrast, for the LCP probe, the distributions show the opposite behavior. The experimental PADs for $\Delta N = \pm 2$ are somewhat more isotropic than the theoretical distributions, which may be a result of the blended pump transition, and the theoretical distributions are only somewhat less "p-like" than those for the $\Delta N = 0, \pm 1$ processes. (Of course, some of the $\Delta N = \pm 2$ "p-like" distributions are oriented along the propagation direction and some are oriented perpendicular to it.) The pronounced polarization-dependent changes in the $\Delta N = \pm 2$ photoelectron angular distributions reinforces the polarization-dependent changes observed in the rotational branching ratios for the same pump transition. The agreement of the experimental PADs with the PADs calculated by using previously extracted parameters is also gratifying. Clearly, the pump transition creates an aligned excited state sample that displays considerable circular dichroism in $\Delta N = \pm 2$ photoelectron peaks.

The photoelectron angular distributions shown in Figure 6 for the $Q_{11}(16.5) + P_{21}(16.5)$ pump transition show considerably less circular dichroism than those for the $R_{11}(14.5) + Q_{21}(14.5)$ pump transition, but the theoretical and experimental distributions are still in excellent agreement. As in Figure 5, the distributions in Figure 6 for the $\Delta N = 0, \pm 1$ processes are predicted to be p-like and oriented perpendicular to the laser propagation direction. The experimental distributions for $\Delta N = 0$ and $+1$ agree well with the predictions. The experimental PAD for $\Delta N = -1$ shows four-fold symmetry, with minima both along the propagation direction and perpendicular to it. This effect is not seen in the predicted PADs. We believe this is due to a weakness in the lower part of the imaging detector, which reduces the signal in a portion of the bottom of the image. This reduction is transferred into the top of the image during the symmetrization that is part of the image reconstruction, resulting in the four-fold symmetry. This deficiency most significantly affects the $\Delta N = -1$ peak, which is the weakest feature in the image. The experimental photoelectron angular distributions for the $\Delta N = \pm 2$ transitions in Figure 6 are much more isotropic than those for the $\Delta N = 0, \pm 1$ processes. Specifically, the $\Delta N = \pm 2$ angular distributions show four-fold symmetry and are almost square. While careful inspection of the $\Delta N = \pm 2$ angular distributions does reveal some circular dichroism for LCP vs. RCP probe light, the effect for the $Q_{11}(16.5) + P_{21}(16.5)$ pump transition is much smaller than for the $R_{11}(14.5) + Q_{21}(14.5)$ transition.

Figure 7 shows the photoelectron angular distributions obtained via the $R_{11}(14.5) + Q_{21}(14.5)$ and $Q_{11}(16.5) + P_{21}(16.5)$ pump transitions using linearly polarized pump and probe beams. We note that the laboratory frame Z axis is along the beam propagation axis for circular polarization and perpendicular to this axis (along the polarization axis) for linear polarization. Both the experiment and theory show significant differences for the photoelectron angular
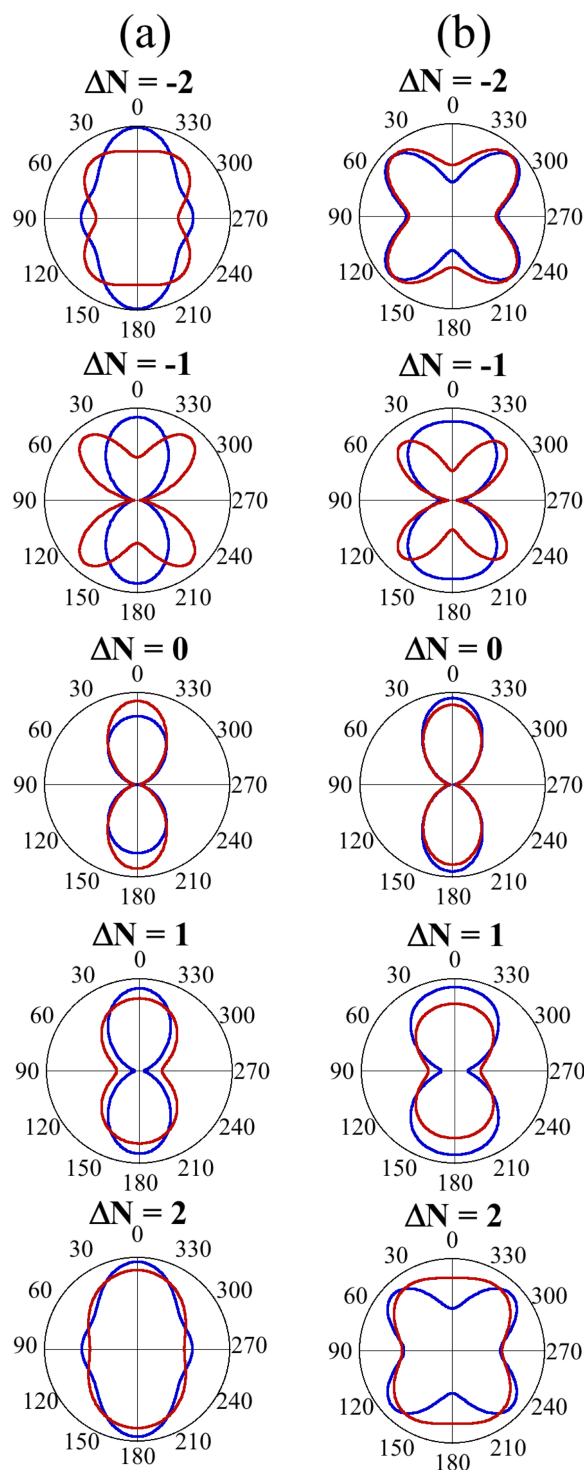

FIG. 7. (a) The PADS following excitation via the A $^2\Sigma^+$, v' = 0 ← X $^2\Pi$, v'' = 0, $R_{11}(14.5) + Q_{21}(14.5)$ transition and ionization at 326 nm with the polarization of the pump and probe beams being linear and parallel to each other. The experimental distributions are shown in red and the theoretical distributions are shown in blue. (b) The PADS following excitation via the A $^2\Sigma^+$, v' = 0 ← X $^2\Pi$, v'' = 0, $Q_{11}(16.5) + P_{21}(16.5)$ transition with ionization at the same probe wavelength and the same polarizations of the pump and probe.

distributions for the two pump transitions. As in Figures 5 and 6, the experimental and theoretical distributions are in excellent agreement for all but $\Delta N = -1$ process, which is likely affected by the same detector issue discussed for Figure 6. Also, as might be expected, the PADs for the

$Q_{11}(16.5) + P_{21}(16.5)$ pump transition are very similar to those recorded previously by using parallel, linearly polarized pump and probe beams by Allendorf *et al.* for the $Q_{11}(22.5) + P_{21}(22.5)$ pump transition.[12]

V. CONCLUSIONS

The present experiments show that CDAD experiments in which ion states are rotationally resolved can be successfully performed using velocity map imaging techniques. The experiment is considerably simpler than the original CDAD experiment,[10,11] in which an angle-resolved spectrometer was used and spectra had to be recorded for multiple polarization/detection angles. However, we note that in the present experiments we are not sensitive to the signs of the phase differences between photoelectron partial waves. There are two significant aspects of the present results. First, the agreement is excellent between the experimental results and the theoretical results based on photoionization parameters extracted in a previous study. This observation provides added confidence to both the present and previous measurements. Second, some pump transitions in the present study result in considerably larger CDAD effects than others. This observation reflects the dependence of the intermediate state alignment and orientation on the pump transition. The resulting CDAD signal shows up very strongly only in the rotational peaks corresponding to $\Delta N = \pm 2$ processes. It is noteworthy that these photoelectron peaks are relatively weak. Thus, in the case of NO A $^2\Sigma^+$, if the CDAD signal was measured in a rotationally averaged manner, the resulting signal would be quite small. In the general case, the dependence of the CDAD signal on the ion rotational state will be controlled by the ionization dynamics of each particular molecular system. In principle, there are a number of molecules that have sufficiently large rotational constants to allow rotationally resolved studies of circular dichroism with photoelectron imaging, for example, many first row diatomic molecules, water, ammonia, and acetylene.

Photoelectron circular dichroism (PECD) is currently being developed as a powerful tool for the study of chiral systems.[1–3] Both single-photon and multiphoton schemes have been developed to make such measurements, and pump-probe time-resolved techniques are also being developed to evolution of chirality upon fragmentation. The present experiments serve as a reminder that the pump process can also induce a dichroism signal in the photoelectron angular distributions. This affects the interpretation of PECD experiments on chiral molecules. In particular, multiphoton experiments on chiral molecules will produce additional dichroic effects caused by the intermediate (or virtual) state alignment. However, whereas the chiral PECD effect results in a forward-backward asymmetry in photoelectron angular distributions, the dichroism resulting from a prepared alignment preserves this symmetry but will appear in other features of the PADs.

SUPPLEMENTARY MATERIAL

See supplementary material for both raw and reconstructed photoelectron images recorded for all three polarization configurations (LCP + RCP, LCP + LCP, and LIN + LIN) following excitation via the overlapped $Q_{11}(16.5) + P_{21}(16.5)$ transitions.

[1] M. Janssen and I. Powis, Phys. Chem. Chem. Phys. **16**, 856–871 (2014).
[2] L. Nahon, G. A. Garcia, and I. Powis, J. Electron Spectrosc. Relat. Phenom. **204**, 322–334 (2015).
[3] S. Beaulieu, A. Ferre, R. Geneaux, R. Canonge, D. Descamps, B. Fabre, N. Fedorov, N. F. Legare, S. Petit, T. Ruchon, V. Blanchet, Y. Mairesse, and B. Pons, New J. Phys. **18**, 102002 (2016).
[4] N. Chandra, Phys. Rev. A **39**, 2256–2259 (1989).
[5] D. J. Leahy, K. L. Reid, and R. N. Zare, J. Phys. Chem. **95**, 8154–8158 (1991).
[6] B. Ritchie, Phys. Rev. A **13**, 1411–1415 (1976).
[7] N. A. Cherepkov, Chem. Phys. Lett. **87**, 344–348 (1982).
[8] I. Powis, J. Chem. Phys. **112**, 301 (2000).
[9] R. L. Dubs, S. N. Dixit, and V. McKoy, J. Chem. Phys. **85**, 656–663 (1986).
[10] J. R. Appling, M. G. White, T. M. Orlando, and S. L. Anderson, J. Chem. Phys. **85**, 6803–6804 (1986).
[11] J. R. Appling, M. G. White, R. L. Dubs, S. N. Dixit, and V. McKoy, J. Chem. Phys. **87**, 6927–6933 (1987).
[12] S. W. Allendorf, D. J. Leahy, D. C. Jacobs, and R. N. Zare, J. Chem. Phys. **91**, 2216–2234 (1989).
[13] D. J. Leahy, K. L. Reid, and R. N. Zare, J. Chem. Phys. **95**, 1757–1767 (1991).
[14] K. L. Reid, D. J. Leahy, and R. N. Zare, Phys. Rev. Lett. **68**, 3527–3530 (1992).
[15] K. L. Reid, D. J. Leahy, and R. N. Zare, J. Chem. Phys. **95**, 1746–1756 (1991).
[16] D. J. Leahy, K. L. Reid, H. K. Park, and R. N. Zare, J. Chem. Phys. **97**, 4948–4957 (1992).
[17] F. Aguirre and S. T. Pratt, J. Chem. Phys. **118**, 1175–1183 (2003).
[18] F. Aguirre and S. T. Pratt, J. Chem. Phys. **122**, 234303 (2005).
[19] H. Xu, U. Jacovella, B. Ruscic, S. T. Pratt, and R. R. Lucchese, J. Chem. Phys. **136**, 154303 (2012).
[20] R. Engleman, Jr., Los Alamos Report LA4364, 1970.
[21] C. Amiot, R. Bacis, and G. Guelachvili, Can. J. Phys. **56**, 251–265 (1978).
[22] C. Amiot and J. Verges, Phys. Scr. **26**, 422–438 (1982).
[23] A. T. J. B. Eppink and D. H. Parker, Rev. Sci. Instrum. **68**, 3477 (1997).
[24] G. A. Garcia, L. Nahon, and I. Powis, Rev. Sci. Instrum. **75**, 4989–4996 (2004).
[25] S. N. Dixit, D. L. Lynch, V. McKoy, and W. M. Huo, Phys. Rev. A **32**, 1267–1270 (1985).
[26] S. N. Dixit and V. McKoy, Chem. Phys. Lett. **128**, 49–54 (1986).
[27] H. Rudolph and V. McKoy, J. Chem. Phys. **91**, 2235–2238 (1989).
[28] K. L. Reid, Annu. Rev. Phys. Chem. **54**, 397–424 (2003).